Biophysical Reports

ARTICLE

Single-cell vibration analysis for potential diagnostic applications

Jared J. Topham,[1] Ali Al-Khaz'Aly,[1,2] Salim Ghandorah,[1] Tvara Parikh,[3] Farshad Farshidfar,[4,5,6,*] and Matthias Amrein[1,7,*]

[1]Department of Medical Sciences, Cumming School of Medicine, University of Calgary, Calgary, AB, Canada; [2]Department of Computer Science, Faculty of Science, University of Calgary, Calgary, AB, Canada; [3]School of Interdisciplinary Sciences, McMaster University, Hamilton, ON, Canada; [4]Department of Oncology, University of Calgary, Calgary, AB, Canada; [5]Department of Biomedical Data Science and Institute for Stem Cell Biology and Regenerative Medicine, School of Medicine, Stanford University, Stanford, California; [6]Tenaya Therapeutics, South San Francisco, California; and [7]Department of Cell Biology and Anatomy, Cumming School of Medicine, University of Calgary, Calgary, AB, Canada

ABSTRACT Vibrational frequency profiling (VFP) using optical tweezers has emerged as a promising technique to characterize single-cell behavior for diagnostic applications. These applications include cancer screening, identifying bacterial resistance to antibiotics, and assessing cellular response to metabolic treatments. Previously, we demonstrated that vibrational profiling can successfully differentiate samples in real time using single-cell vibrational signatures. However, the sensitivity of this approach and its ability to be applied across variable experimental conditions and cell lines have not been well identified. This study builds on previous work, demonstrating the feasibility of our established vibrational analysis to quantitively assess whether changes in experimental design can improve model separation of different cell types.U251 human glioblastoma cells and A549 human lung carcinoma cells were used as our model system. We illustrate this capability through three examples: 1) comparing an open Petri dish to closed microfluidic chambers, 2) synchronizing cells in the cell cycle, and 3) altering medium viscosity. These factors were selected for their potential to influence signal quality and model accuracy. Vibrations were collected using optical tweezers, were Fourier transformed to produce power spectra, and were then parameterized using peak detection, extracting area under the curve values. Peaks were aggregated across samples and classified using partial least squares discriminant analysis. Partial least squares discriminant analysis classification was performed with 70/30 train-test splits of data and 10-fold cross-validation.Petri-dishes yielded a more well-classified sample than microfluidics chambers (F1 score 0.89 vs. 0.79). Synchronized cells reduced vibrational variability and improved classification (F1 score 0.83 vs. 0.79). Increased viscosity produced slight classifier improvements (F1 score 0.81 vs. 0.79). These findings demonstrate that VFPs are sensitive to the mechanical and environmental context of cell measurement, highlighting that careful standardization of experimental conditions is crucial for developing reproducible and clinically translatable VFP-based diagnostic platforms.

WHY IT MATTERS Single-cell vibrational profiling with optical tweezers offers a label-free window into cellular mechanics and metabolism with promise for rapid diagnostics. This study demonstrates that the experimental context—including chamber geometry, alignment of cell-cycle state, and the viscosity of the surrounding medium—systematically shapes vibrational signatures and the ability of statistical models to distinguish cell types. By identifying controllable factors that improve separation while reducing variability, the work establishes practical benchmarks for standardizing acquisition and analysis. These insights advance reproducibility and comparability across laboratories and move vibrational profiling closer to clinical applications such as cancer screening and treatment monitoring. Finally, this approach contributes a practical framework to test which factors shape cell vibrations and whether they sharpen discrimination or add noise.

INTRODUCTION

Living cells exhibit intrinsic mechanical vibrations that correlate with metabolic activity, offering potential as biomarkers for disease states (1–9). Single-cell vibrational analysis, particularly through a

Submitted November 17, 2025, and accepted for publication January 14, 2026.

*Correspondence: farshidfar@gmail.com or mamrein@ucalgary.ca

Jared J. Topham and Ali Al-Khaz'Aly contributed equally to this work.

Editor Name: Ulrike Endesfelder

https://doi.org/10.1016/j.bpr.2026.100252

method termed cell vibrational profiling (CVP), captures these oscillatory patterns using force-spectroscopy techniques such as atomic force microscopy (AFM) and optical tweezers (OT) (1–9). This technique carries applications in understanding metabolic diseases and using cellular oscillations as cancer biomarkers, among others (1–9). Although these force-spectroscopy methods remain foundational, the toolkit for detecting cellular oscillations contains highly innovative approaches. For instance, Willaert et al. demonstrated that classical optical microscopy can be adapted for optical nanomotion detection as a widely accessible means to monitor the nanomotion of nonattached cells (10). Conversely, pushing the limits of mechanical sensitivity, Rosłoń and colleagues utilized suspended graphene nanodrums to probe single bacterium nanomotion with ultrahigh precision, revealing new insights into the origins of cellular vibrations (11). Together with AFM and OT, these diverse detection modalities underscore a growing versatility in the acquisition of vibrational analysis. To maximize benefit from these advancing acquisition methods and enhance the reproducibility and diagnostic reliability of CVP, here, we have examined key experimental parameters that influence cell vibrational profiles.

Single-cell force spectroscopy studies examining biological vibrations are a growing field (1–8). The behavior of cells in the context of bacterial resistance to antibiotics, movements of the cytoskeleton, and treatment of brain tumors have been studied using force spectroscopy, primarily OT and AFM (2,4,5). OT and AFM measure oscillations of a cell inside of controlled potentials (12). Cells inside of these potentials move and vibrate due to metabolic activity and a variety of intracellular processes, providing insights into its mechanical behavior and a rich array of cell-line-specific information. Oscillations, initially measured as cellular displacement, are calibrated to produce meaningful force-time outputs (13–15). Although the precise origin of these vibrations is not yet understood, theoretical models have predicted, and experiments using human breast epithelial cells attached to microcantilevers have confirmed, the existence of cell-specific vibrational patterns (16). Distinguishing cells based on oscillatory patterns has successfully achieved discrimination of mitochondrial activity, screening of antineoplastic drugs, and antibiotic susceptibility testing, as well as identifying different stages of an oocyte's development, highlighting real clinical potential for mechanical phenotyping using CVP (1,6–8). These foundational investigations have not only established the experimental basis for CVP but have also demonstrated its potential for distinguishing disease-specific mechanical phenotypes with high sensitivity. However, reproducibility and reliability of vibrational data remain challenged by experimental variability and a lack of a unified experimental approach to cell vibrations, thereby necessitating rigorous control of measurement conditions (9,17,18). Improvements in experimental protocols, the subject of the current paper, are therefore crucial to further establishing the reliability of CVP. This study investigates the impacts of three key factors on cell vibrations: experimental chamber configurations, cell medium viscosity, and cell cycle phases. In evaluating these different conditions on oscillatory spectra, it is fundamental to the method's design to also evaluate their impact on improving group differentiation.

Here, we explored two forms of sample chambers, closed top (microfluidic channels) and open top (Petri dish style). Closed-top microfluidic chambers effectively shield cell samples from external forces found in the environment directly above the sample, in comparison to traditional open-top cell culture dishes. Methodologically, it is imperative to understand if experimental factors such as choice of chamber affect the comparisons of cell types and create a source of data variability.

When examining a cell trapped in a harmonic potential, as in force spectroscopy, the presence of Brownian motion has been widely recognized (12,19–21). Brownian motion refers to random movement resulting from thermal fluctuations of particle (either liquid or gaseous) collisions (20). Brownian motion randomly contributes background noise to force spectroscopy signals and is Gaussian in nature. This random contribution of background noise can cloud recordings and obscure extraction of true internal vibrations (9,17). It is further complicated as Brownian motion is utilized by cells via Brownian motors, whereby random noise is employed by cells to achieve directed movement (22). The size of the cell, viscosity of the fluid, and temperature all affect Brownian motion (23–25). Therefore, we examined whether changes in medium viscosity can serve as a theoretical clamp for cells in CVP experiments, shielding them from the impacts of Brownian motion. In a viscous medium, or a medium with a high loss modulus, vibrations that are produced by any source are likely to be rapidly dissipated in an overdamped manner, rather than oscillate as they would in less viscous media. It is crucial to understand that interplay exists between Brownian motion, cellular activities, and viscosity in terms of cell micromechanics.

Depending on the stage of the cell cycle, cellular metabolic activity may be altered (26,27). It has been observed that metabolic activity occurring in a cell at a given point in time is often linked to cell-cycle

events, like mitotic exit and budding (26). This finding in eukaryotic cells suggests a level of synchrony between metabolic activities and the corresponding phase of the cell cycle. This was further examined in mammalian HeLa cells, where 57 different metabolites oscillated in response to different stages of the cell cycle (27). In the case of diagnostics, the impact of cell-cycle stage is unknown, and synchronization is not performed. Yet, diagnoses and profiling of cells are two of the primary intended applications of cell vibrational analysis (2,3,8). In these cases, it is imperative to understand how results are impacted by the heterogeneity of cell-cycle stages in the sample and how this can affect downstream diagnoses. Therefore, we sought to investigate whether cells within different stages of the cell cycle can be differentiated from each other based on their vibrational profiles. If cells synchronized in the G_0/G_1 phase can be differentiated from unsynchronized counterparts, this may have methodological implications on CVP.

CVP was utilized as a statistical approach for assessing cellular differentiability across experimental conditions. Traditional approaches to spectral analysis primarily emphasize feature extraction; however, they may be susceptible to interpretation or conformation bias. Al-Khaz'Aly et al. provided a technique by which signals are Fourier transformed, enabling extraction of a distinct vibrational frequency profile (VFP) from the set of all detected frequencies rather than emphasizing any individual frequency (9). This approach avoids overexamination of unique frequencies and instead examines whether differences can be established based on VFPs (9). It then employs the data-driven statistical approaches of partial least squares discriminant analysis (PLS-DA) and principal component analysis to determine whether groups of cells can be differentiated and the significance of experimental conditions.

We found that across all experimental groups, successful differentiation was achieved with varying levels of precision. The F1 score is a metric used in machine learning to evaluate the performance of a classification model. When comparing closed-top microfluidics and open-top dished sample chambers, F1 scores of 0.79 and 0.89 were obtained, respectively. Next, comparing cell-cycle-synchronized to unsynchronized samples, we observed F1 scores of 0.83 and 0.79, respectively. Finally, we compared cells in viscosity-increased medium versus untreated controls and observed F1 scores of 0.81 and 0.79, respectively. Here, we present a technique to measure the relative impact an experimental condition has on findings, and we find that these results support the hypothesis that all experimental considerations should be put into place, and inconsistency in these experimental conditions can be a source of nonuniformity when comparing data recordings.

MATERIALS AND METHODS

Cell culturing

Human alveolar epithelium (HAE) cells, A549, were the primary cell line utilized in this study, which were then compared with U251 human glioblastoma multiform (GBM) cell lines. This pair of cells was chosen due to their distinctly different purposes, high metabolic activity and short doubling time, making them representative of rapidly proliferating cancer cells (28). Cells were cultured in Dulbecco's Modified Eagle Medium (DMEM) (Gibco, Lot No. 2257195, Ref. No. 11995-06) containing 10% fetal bovine serum (FBS) and 1% penicillin streptomycin (Corning; Lot No. 30002317) in T75 flasks. Before experiments, cell medium was aspirated from T75 flasks and then subsequently washed with 5 mL of Dulbecco's Phosphate Buffered Solution (PBS) (Gibco; Lot No. 2070590, Ref No. 14190-136). PBS was aspirated out of the flask, and 3 mL of 0.25% trypsin was added. Cells were dissociated by incubating the flask in an Accumax TM CO_2 chamber for 3 min at 37°C. The 3-mL dissociated cell/trypsin mixture was transferred from the T75 flask to a 15-mL test tube where 7 mL of fresh culture medium without growth factor was added. The 10-mL sample solution was centrifuged for 10 min at 1200 RPM. After centrifugation, the cell medium was aspirated from the cell pellet. 10 mL of cell culture medium was added to resuspend pelleted cells. 9 mL of the sample medium was transferred into a new T75 flask for cell culturing, and 1 mL of the sample was diluted in an additional 19 mL of fresh medium. From that aliquot, 2 mL of the cell-medium mixture was pipetted either into a 35-mm μ-Dish TM (Ibidi, Germany) for dished samples or 60 μL into a 0.4-mm Luer uncoated Ibidi channeled μ-slide (Ibidi, Germany) for microfluidics samples, depending on the experimental setup. All samples were maintained at 37°C throughout experiments to ensure consistency. Cell viability was assessed before experiments using AlamarBlue, and cell viability was found to be >91% in all experiments (19).

The dimensions of the microfluidic slides consisted of an outer dimension of 25.5 × 75.5 mm^2, with a #1.5 polymer coverslip enclosing the channel. The channel itself measured 5.0 × 50 mm^2 as width and length of the channel, and the overall height of the slide was 9.5 mm. For dished samples the dimensions consisted of a #1.5 polymer coverslip enclosing a 35-mm-diameter Petri dish.

Cell synchronization

To determine the effect of cell synchronization on the VFP of cells, we employed serum deprivation to align A549 cells in the G_0/G_1 phase of the cell cycle. To synchronize cells in the G_0/G_1 phase, a serum deprivation protocol was adapted from Lauand et al. (29). A549 cells were gradually serum-starved over several days and ultimately incubated in DMEM with 0% FBS for 50 h. After 50 h, cells were seeded in DMEM with 10% FBS and 1% PS to allow cell progression through the cell cycle (the process from G_0/G_1 to G_2 for this cell type is cited to take around 46 h, allowing ample time to take oscillatory measurements). From there, cells were transferred to microfluidic chambers for use in the OT.

Viscosity experiments

To examine how the viscosity of surrounding medium affected measurements of cell oscillations using the OT, we compared

A549 cells in DMEM in comparison to the same medium with incrementally increased viscosities. We employed four different experimental conditions. Group one employed standard DMEM with 10% FBS and 1% PS. Group two had its medium viscosity increased by adding 0.1 wt % (g/mL) of agarose (Life Technologies; Cat. No. 15510-019, Lot No. 1AP6465). The third group, which also shared the same DMEM, had its viscosity increased by adding 0.2 wt % (g/mL) of agarose. Finally, the fourth group had its viscosity increased by adding 0.3 wt % (g/mL) of agarose. All samples were examined in microfluidic chambers.

Agarose was used as it minimizes the impacts to medium osmolarity while still increasing viscosity, and it is a commonly available agent. Agarose is primarily used as a gelling agent in cell culture and molecular biology applications with applications in gel electrophoresis (30).

The protocol for mixing agarose with the medium is described below. First, the agarose, hereby known as the solute, was blended within a medium solution containing no cells at an amount of either 0.1, 0.2, or 0.3 wt % in a slow fashion to avoid the formation of aggregates or bubbles. For the two conditions, we employed either 0.02 g or 0.06 g of agarose in 10 mL of DMEM. The solutions were heated to 100°C or until all the agarose was dissolved. The medium-agarose solutions were sterilized in an autoclave at 10–15 pounds of pressure for 10–15 min. 10 mL of the cell culture medium (containing the A549 cells in DMEM with 10% FBS and 1% PS) was unified with the medium-agarose solutions once they had cooled to 37°C. Aliquots of these solutions were transferred into microfluidic cell chambers and taken to the OT for measurement. To measure the apparent viscosity of these different groups, we dropped a metal marble of known weight and radius down a graduated falling-ball viscometer and measured the time it took to reach the bottom, and viscosity was calculated and compared with existing standards. Viscosity measurements took place at a temperature range from 35°C to 37°C.

Optical tweezers

Experiments were conducted using the Nanotracker 2™ (Bruker) OT system. Viable, isolated cells were trapped using a 500-mW laser. Single-cell force spectroscopy using OT examines vibrations emitted by a singular cell trapped in a Gaussian distribution of laser intensity (26). Particles trapped within OT experience antagonistic gradient and scattering forces, which trap the particle in a three-dimensional space at a place of net zero force (13,14). Within the laser, the cell vibrates and causes deflections in the laser beam whereby the beam of light applies an equal and opposite force to the cell to maintain the trap, and these changes in laser intensity can be detected using a position sensitive quadrant photo detector (QPD) system (31). The detected light beam oscillates relative to cell vibrations, and changes to the distribution of light intensity are detected by the QPD (26). The light-sensitive material of the photo detector of the QPD converts energy contained in photons of the laser into photocurrent and electrical signals relative to the intensity of incident light (32).

Experiments consisted of 15 second recordings with a stationary laser at a sampling rate of 100,000 Hz. Before each experimental recording, the quality of the trap was assessed using a drag test as described in the Supporting Material (Fig. S1).

Metrics for raw data

In the past, approaches using AFM have largely used cantilever deflection to compare the intensity of vibrations in a recording and calculate variance in cantilever deflection across samples (1,3,4,6,7). As no cantilever is involved in OT systems, researchers opt for root mean-squared (RMS) values to compare overall power across recordings and as a measure of centrality within a recording. The RMS of a signal of n discrete data points is summarized as follows (33):

$$RMS = \sqrt{\frac{1}{n}\sum_{i=1}^{n}(x_i)^2}$$

RMS is a commonly used metric to examine overall signal power and changes in power when compared across different time measurements (33). RMS calculations were performed automatically using Python code.

Another metric used was the coefficient of variation, a unitless statistic that measures data spread by dividing standard deviation by mean, often expressed as a percentage. Because this ratio standardizes variability, it allows direct comparison of how data sets spread despite different means. Furthermore, the frequency domain provides an intuitive understanding of the distribution of power across the frequency spectrum. Several AFM-based studies have included examinations of the frequency domain (1,2). The frequency domain decomposes the raw time domain signal into its constituent frequencies using a Fourier transform (30). From the Fourier-transformed signal, one can then extract the phase and power spectrum (30). In our study, there was concern about the distribution of power at different frequencies, and therefore, we employed power spectra (PS). To obtain a PS representative of a population, we determined that for each time point, the median was reconstructed into a new median time domain signal. Median values are more robust than mean values when analyzing data that may contain outliers (34). This median signal for each population was then Fourier transformed. The signal was then squared to obtain power spectra. Code used for obtaining the RMS of time domain samples and Fourier transforming the final median time domain data was performed in Python and can be found in the Supporting Material.

Statistical analysis

Significant amounts of vibrational information may be derived from the frequency domain. We previously provided a technique to examine vibrational activity in the frequency domain and associate samples to distinct frequencies using peak detection on power spectra as predictors in multivariate statistical analysis (9). Here, we have adapted this approach whereby, rather than splitting long data recordings into shorter segments, short data recordings were directly collected (9). This allowed for an increased sample size with larger numbers of cells examined. We then emulated our previous procedure as outlined, performing Fourier transformation to extract a frequency domain spectrum, which is then peak detected and parameterized (9). We utilized the Z-score-based peak detection algorithm (9,35). Parameterized peaks were then used as features in PLS-DA modeling to establish differentiation between samples under different conditions. A PLS-DA predictive model was developed for each of the chamber, viscosity, and cell-cycle synchronization experiments, respectively.

All data collection was performed for 15 s, with a frequency resolution of 0.067 Hz and a resolvable spectrum of 50,000 Hz by the Nyquist theorem (36). To preprocess, all peaks detected within 100 Hz of each other were aggregated to account for variation and peak-shift tolerance across experiments. Parameterized peak frequency and area under the curve (AUC) values were tabulated into a matrix. This provided a table of all the different peaks, with their frequencies and respective AUC values detected across all

samples. Data samples were then split into 70% training data and 30% testing data with stratification for each class of input. Data were scaled using unit variance, known as autoscaling, accounting for differences across samples. Scaling was done per sample, whereby the peaks detected within a recording were scaled against each other. Autoscaling is important, as when variables in a data set have significantly different levels of intensity and variability, PLS-DA and other multivariate methods will predominantly concentrate on a limited number of variables that exhibit the strongest signals (32,33,37). This common approach is used in metabolomics where variables can have vastly different ranges, potentially leading to some variables dominating the model due to their larger values (32,33,38).

PLS-DA was chosen as our discrimination method as a technique that provides dimensionality reduction by projecting data onto a new space of latent variables (29,39). This makes PLS-DA effective at handling data with multicollinearity and high dimensionality, which has played an essential role in its adoption in metabolomics studies (33). Considering input data will provide a new dimension for each peak frequency, this may result in hundreds of peaks found across a spectrum and therefore hundreds of dimensions that are not easily comparable, making it essential to have a dimensionality reduction technique like PLS-DA (34,40). Furthermore, PLS-DA is a supervised method whereby label information is provided to the model, and when combined with cross-validation (CV), it helps to mitigate the risk of overfitting to training data (29,39). PLS-DA works to preserve as much covariance between input data and the labels as possible, with the most covariance captured in the first component, whereby the variance of the component is then removed or peeled from the data set, and the next component is computed on this new residual matrix, a process that repeats for all components (40).

PLS-DA was performed using the "kernelpls" fit method using the plsr function, available from the Comprehensive R Archive network (41). PLS-DA models were cross-validated using 10 randomly generated folds applying validation groups from training data when selecting model complexity in root mean-squared error in prediction (RMSEP) plots. Considering that peaks in the power spectrum were parameters of the model, the maximum components in all PLS-DA models were the number of detected peaks, minus 1. The ideal number of components to retain in the PLS-DA model was determined using the RMSEP plot, by selecting minimum RMSEP values for each of the output classes, as is common practice for PLS-DA component selection (41,42). For each component number, the model with that number of components was predicted on 10-fold validation data and generated a CV and bias-corrected CV value (41). Bias correction in RMSEP values is important as CV can underestimate the true prediction error due to the model being trained on a slightly smaller data set than the full training set (36,43). Bias correction of RMSEP values was performed automatically using the pls library (41).

For multiclass data, a "one-vs-all" approach was utilized for training, model tuning, and metrics. One-vs-all consists of an output variable assigned to each class label; for any given sample recording, only one of the output variables will be "1" (the true label), and the remaining variables are assigned "0" (false labels). Considering that PLS-DA is regression with categorical response variables, there needs to be a technique to convert continuous numerical output to class predictions. The technique used to achieve this is decision boundaries (34). An ideal decision boundary was selected using precision-recall (PR) curves, testing multiple different boundaries. This approach is particularly reliable when dealing with imbalanced data sets, where the number of samples of each output category is not equal (44). This preferentially utilizes PR curves for the decision boundary over the use of a receiver operating characteristic curve (44). The decision boundary was chosen from PR curves with a balanced approach between precision and recall, but with a slight preference toward recall, ensuring that models are not only accurate in identifying positive instances but also effective in capturing most true positives. This is crucial in scenarios where false negatives carry significant costs, such as CVP, whereby the ability of the model to identify cancerous cells from a sample of cells is one of the intended goals.

Metrics extracted from the model were obtained by predicting the model with the selected number of components on test set data and extracting the predicted classification using the decision boundary. F1 score was the preferred metric for this application as it typically performs better than accuracy on data sets that have imbalanced classes (34). In those cases, accuracy can be a misleading and misrepresentative metric (34). F1 score is described by the below equation:

$$F1 = 2 * \frac{Precision * Recall}{Precision + Recall}$$

F1 can be described as a balanced measure of a model's performance by considering both the number and quality of accurate predictions by accounting for both precision and recall. In the context of cell vibrational experiments comparing a cancerous and noncancerous experimental group, a high F1 score (closer to 1) would demonstrate that the model has both a high capability of identifying cancerous cells (recall) and does so with a small number of false positives (precision).

All computation was performed in R using RStudio on a program referred to by Al-Khaz'Aly et al. as the Vibration Scanner Analysis Suite (VSAS) (9). The machine used to perform data processing was an Intel Core i7-13700KF with 128 GB of random-access memory.

RESULTS

We examined three different conditions, including different chamber geometry, synchronized cell-cycle states, and increased medium viscosity to disentangle environmental from biological contributors to the vibrational signal. We probed chamber-dependent resonance, biological heterogeneity through cell-cycle synchronization, and reduced Brownian motion interference through viscosity.

Raw data analysis

VFPs of A549 cells in closed cavity microfluidic channel slides (Fig. 1, red) versus open-cavity Petri dish (Fig. 1, blue) conditions were analyzed. Analysis included RMS values, raw force-time signals, and power spectra (PS) from 15-s cell recordings (Fig. 1).

Sample chamber comparison: Microfluidic versus dished

For sample chamber experiments, A549 cells were recorded in microfluidic ($n = 173$) and dished chambers ($n = 129$), with one microfluidics recording omitted due to data being corrupted. RMS values were tabulated for each recording, and a Welch's unpaired *t*-test revealed a significant difference in values

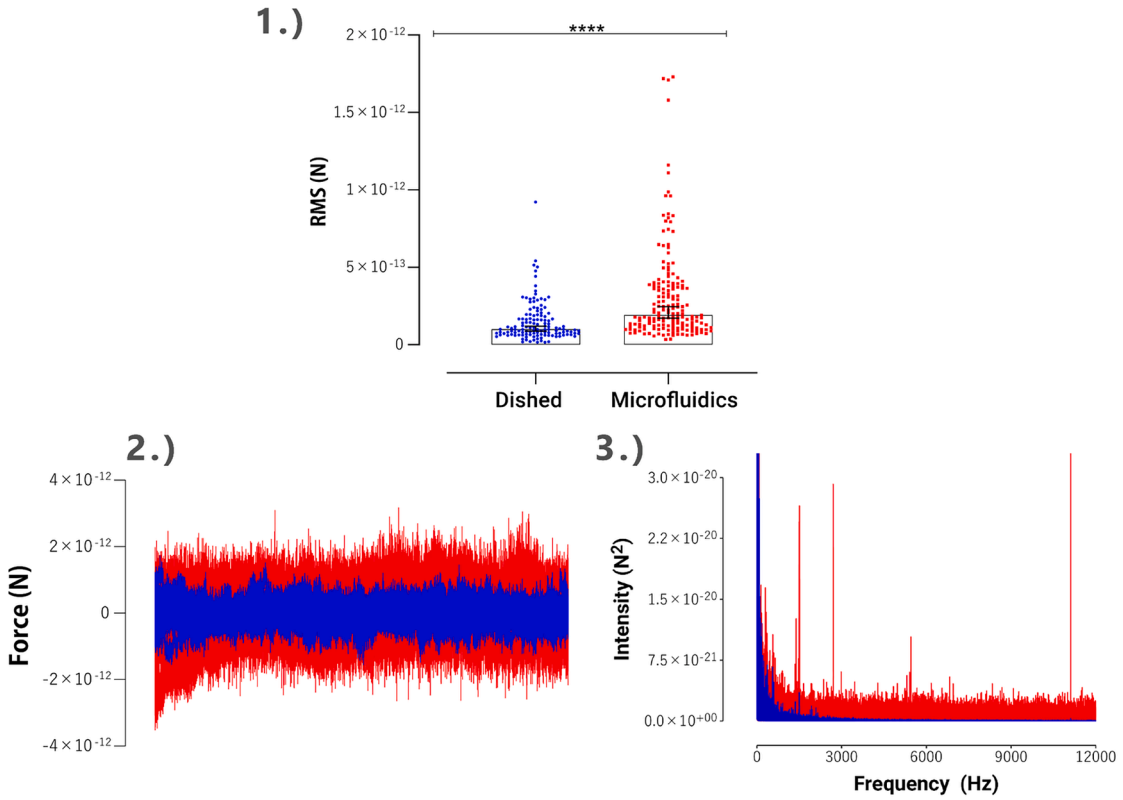

FIGURE 1 The effect of the sample chamber on the vibrational signal. (*1*) RMS comparison of A549 cells in 2-mL Ibidi cell dished (*blue*; $n = 129$) and 60-μL microfluidic cell chamber (*red*; $n = 173$) conditions. Both conditions received the same DMEM with 10% FBS and 1% PS. RMS was measured as a function of the force of the recording for that specific cell condition, *'s are indicative of degrees of significance values from Welch's unpaired *t*-test. Error bars represented median with 95% CI, where median was chosen to display as it is less susceptible to outliers than mean values. (*2*) A 500-ms representative oscillatory signal was adapted from three 15-s scans illustrating amplitudes (N) of each condition. (*3*) Power spectra displaying how the change in experimental chamber impacts the findings in the frequency domain for VFPs of A549 cells. The entire 50,000-Hz spectrum is displayed.

between the two groups (*p*-value < 0.0001 and *t*-score of 6.223) (Fig. 1.1). Microfluidic samples showed higher vibration intensity (median RMS = 1.90e−13 N) compared with dished samples (median RMS = 9.92e−14 N).

The raw force-time domain analysis for microfluidics and dished A549 cells displayed the average intensity of the force signal over a 1-s time frame (Fig. 1.2). Microfluidic cell conditions exhibited the highest average oscillatory signal with maximum and minimum values of 3.26e−12N and −3.42e−12N, respectively. In contrast, dished cell conditions showed reduced amplitude with maximum and minimum values of 1.79e−12N and −1.47e−12N, respectively.

All raw signals were averaged and Fourier transformed to generate a single PS for analyzing power contained within each frequency (Fig. 1.3). The two plots were then overlayed in Prism (GraphPad Software) for comparison. Differences were most pronounced below 15,000 Hz, with a notable spike at 11,000 Hz (Fig. 1.3). At low frequencies the graphs did not consistently follow the same shape, but dished PS contained substantially more power than microfluidic samples. Above 15,000 Hz, the difference between the two populations became less evident (Fig. 1.3).

PLS-DA classification: Sample chamber comparison

We aimed to identify the experimental conditions in terms of sample chambers that best improve differentiation in CVP experiments. To achieve this, each condition was compared against a separate cell line as a control (U251) to identify the condition that maximizes differentiation. To establish statistical differentiation between sample classes, the VSAS was used as described in the materials and methods and in the literature (9). PLS-DA models were developed on frequency peaks automatically picked from power spectra, whereby AUC values for each detected frequency peak were parameterized and used as a feature in the PLS-DA model.

Two separate PLS-DA models were developed (Fig. 2). One was trained on 173 A549 cells in

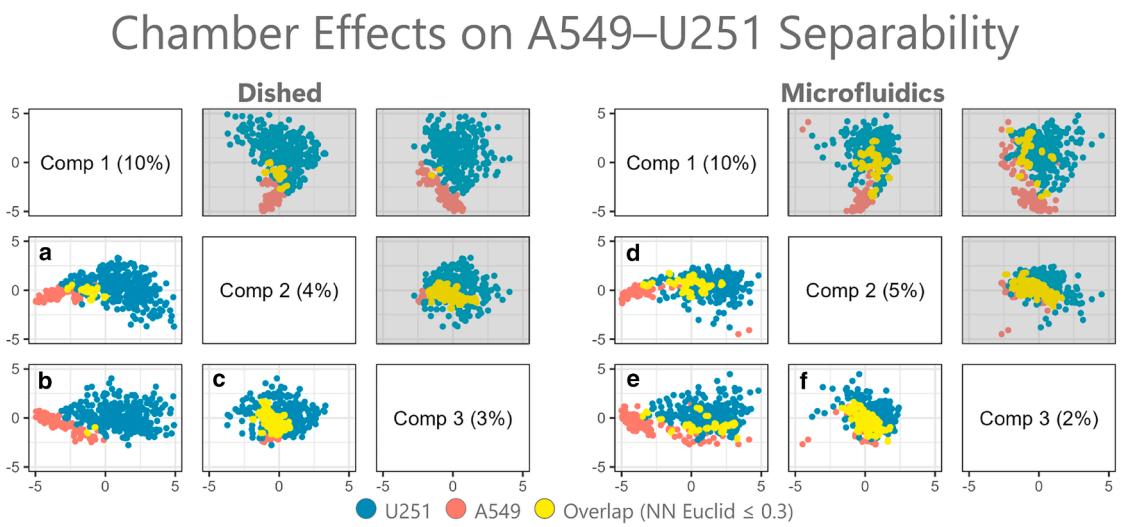

FIGURE 2 PLS-DA score-plot matrices comparing A549 (*red*) and U251 control (*teal*) single-cell vibrational recordings. A549 recordings were acquired in dished (*left*) and microfluidic (*right*) environments. Separate PLS-DA models were fit for each condition. Each point represents one 15-s cell recording. Diagonal tiles report the component number and percentage of variance explained by the component. Off-diagonal tiles show pairwise score plots; labeled panels (*a–c* and *d–f*) correspond to the unique component pairs in the dished and microfluidic models, respectively. Gray background tiles are mirrored duplicates of the labeled comparisons with axes transposed. Yellow points indicate overlap (Euclid $\leq$ 0.3): a point (from either class) is colored yellow if its nearest neighbor from the opposite class lies within 0.3 Euclidean distance in the 2D score space of that panel.

microfluidic chambers and 403 U251 control recordings. The second was trained on 129 A549 cells in dished open-cavity chambers and 403 U251 cell control recordings. Each model contained a training-test split of 70-30 with class-based stratification. This created a testing set containing 172 total samples: 52 microfluidics A549 cells and 120 U251 glioblastoma samples for the first model. The second model had a testing set of 157 total samples: 37 dished A549 cells and 120 U251 glioblastoma cells. In both cases, the aggregation of peaks within 100 Hz of each other was performed, as metabolic activity may have slight variation across different cells, resulting in a total of 167 detected peaks for the dished model and 202 peaks for the microfluidics model.

Scores plots were generated whereby data were projected onto the first three newly developed PLS components (Fig. 2). This was performed to visually examine the similarities and differences in the data and more easily visualize the spread of data as shown by PLS components (Fig. 2).

In both cases, the first three components captured a total of 17% of the model's variance, indicating a small amount of the original data contained meaningful differentiative information used to separate cell types, and much of it could be excluded without losing model differentiation ability. A549 cells (red) exhibited pronounced dispersion along the negative axis of component 1, creating a characteristic tail-like pattern extending far from the origin (Fig. 2, *a*, *b*, *d*, *e*). This spread, demonstrated along the first component, accounted for 10% of the total variance whereby A549 cells and U251 GBM cells were visually distinguished (Fig. 2, *a*, *b*, *d*, *e*). Generally, U251 cells (teal) demonstrated more centralized clustering around the origin but still displayed dispersion throughout all three components, especially the third component (Fig. 2, *b*, *c*, *e*, *f*).

When examining the interaction between components 2 and 3 on both conditions, the cell types demonstrated considerable spread across both positive and negative values, but it was difficult to distinguish the two cell types due to substantial overlap when using components 2 and 3 alone (Fig. 2, *c* and *f*). Comparing the two conditions, along the second component in the microfluidics condition (Fig. 2 *f*), a pair of two A549 samples separated from the major concentration of A549 samples. This separation was only captured in the second component. In the microfluidics condition, we observed the cluster of red A549 cells was less tightly grouped than the dished condition and spread into the positive portion of the axes along the third component's intersection with the first. This suggests A549 cells in culture dishes yielded a more uniform cellular response and provided a more differentiable sample population pattern (Fig. 2).

The variable importance in projection (VIP) plots were used to observe the relative impact of vibrational frequencies. For each condition the hierarchy of frequencies was observed. For microfluidics, 338 Hz, 1480 Hz, and 1540 Hz were the most pronounced and accounted for over 7.5% of the model's variance (Fig. 3, left panel). The presence of 338 Hz among

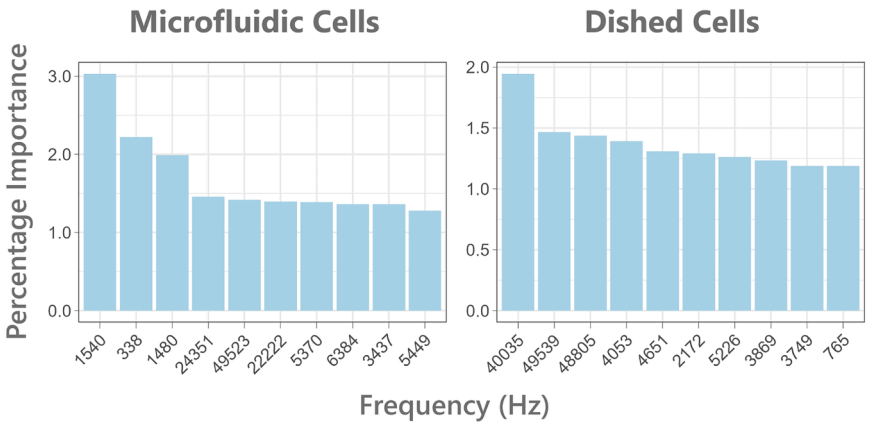

FIGURE 3 VIP plots for the first component of the PLS-DA model comparing microfluidic (*left*) and dished (*right*) A549 cell culture conditions. Each bar represents the percentage contribution of an individual frequency to the overall variance explained by the first component. Microfluidic cells show a pronounced contribution from a small number of frequencies, particularly at 1540 Hz, 338 Hz, and 1480 Hz, indicating distinct vibrational signatures. In contrast, dished cells display a more even distribution of importance across higher frequencies, with the most significant contributions at 40,035 Hz, 49,539 Hz, and 48,805 Hz, reflecting a more uniform vibrational profile.

the top contributors aligns with previous cell vibration research identifying significant activity below 500 Hz (Fig. 3). This pattern demonstrated that microfluid-cultured cells possess distinct vibrational signatures, particularly in the low- and mid- frequency ranges, as shown by the sharp decline in importance beyond the first few frequencies (Fig. 3). In contrast, dished cells exhibit a more uniform distribution of frequency importance, with the highest importance vibrations all concentrated in the 40–50 kHz range (Fig. 3, right panel). The most significant frequency, 40,035 Hz, accounts for approximately 2% of the model's variance (Fig. 3).

The optimal number of components for each PLS-DA model was determined using RMSEP and PR analysis on validation data (Fig. 4). For microfluidic samples, three components minimized the RMSEP (∼0.29), achieving high precision (0.975) and recall (0.943) at a classification threshold of 0.477. For the dished model, two components gave the best RMSEP (∼0.28), with precision and recall of 0.851 and 0.899, respectively, at a threshold of 0.449. Overall, microfluidic samples showed slightly better classification performance in training/validation data than dished samples.

Binary classification was performed to distinguish A549 and U251 cell types under both microfluidic and dished conditions, with A549 cells treated as the positive class and U251 cells as the negative class (Tables 1, 2, 3, and 4). For each model, a confusion matrix was generated to demonstrate the ability of the model to differentiate between samples across different conditions in the test set using its respective threshold (Tables 1 and 3). For microfluidic samples, a total of 172 test set samples, containing 120 U251 samples and 52 A549 microfluidic samples were evaluated using a PLS-DA model with three components and a decision threshold of 0.477. Metrics were extracted with microfluidics class as positive (Table 2). Performance metric calculations described an F1 score of 0.79 (Table 2). An F1 score of 0.79 suggested the model performed moderately well in balancing precision and recall. A perfect model would achieve an F1 score of 1.0 (93,94). For the dished samples, 157 test samples were evaluated (120 U251 and 37 A549), using a PLS-DA model with two components and a decision threshold of 0.449. The same evaluation metrics as those used for the microfluidic samples were calculated (Table 4). The dished model outperformed the microfluidics model with markedly better performance, achieving an F1 score of 0.89, a precision of 0.87, and a recall of 0.92 (Table 4). Using vibrational data in CVP, we detected measurable differences in VFPs that allow for development of PLS-DA models to distinguish cell types; moreover, cells cultured in Petri dish environments are more readily differentiated using VFPs than those grown in microfluidic chambers.

Comparative summary: Cell-cycle synchronization and viscosity effects

To provide a comprehensive evaluation of all experimental conditions examined in this study, cell-cycle synchronization and viscosity experiments were also conducted with full methodological details as described in the materials and methods section. Complete raw data analysis, power spectra, VIP plots, RMSEP curves, PR analyses, and scores plots for these conditions are available in the Supporting Material (Figs. S2–S9). We present the key classification performance metrics to enable direct comparison across all experimental conditions.

Cell-cycle synchronization

A549 cells synchronized in the G_0/G_1 phase through serum deprivation in microfluidic chambers ($n = 105$) were modeled against U251 control cells ($n = 403$). Synchronized cells demonstrated reduced vibrational

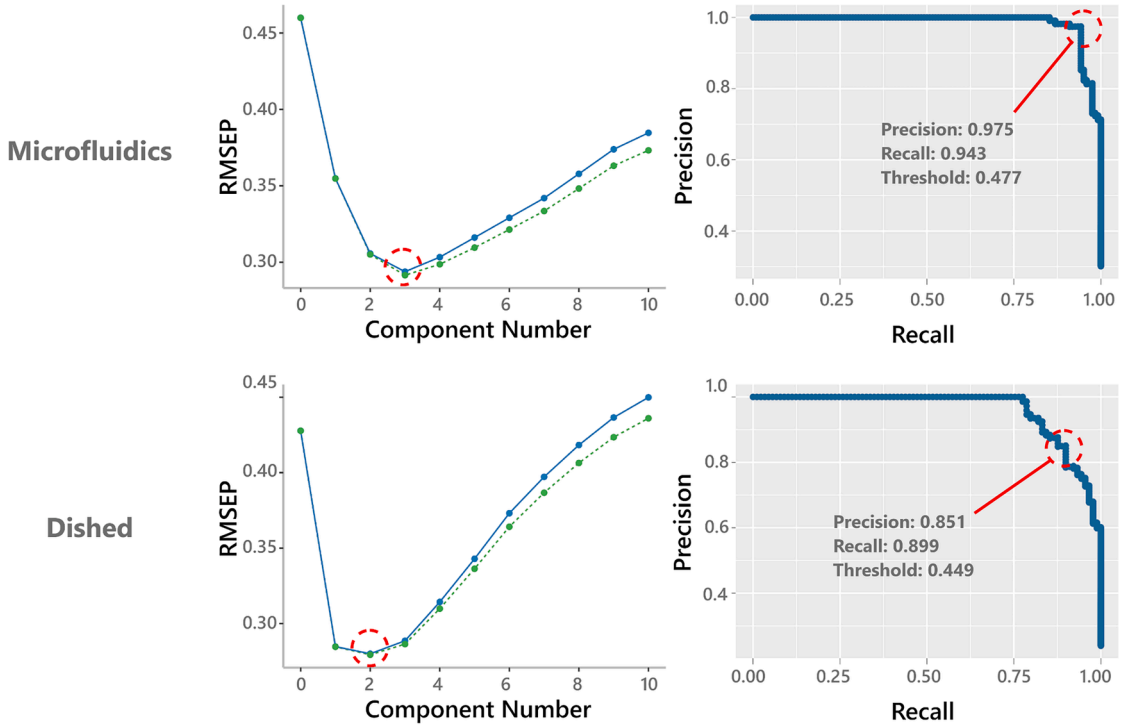

FIGURE 4 Model tuning plots of RMSEP and PR for dished versus microfluidics samples. RMSEP and PR curves were generated from 10-fold CV data. Displayed plots are for microfluidic (*top*) and dished (*bottom*) samples. Left: RMSEP curves demonstrate the error generated on validation data when using a PLS-DA model with an increasing number of components; this is to find the optimal number of components for model generalizability. The blue line represents model RMSEP on 10-fold CV training data, whereas the dotted green line shows bias-corrected estimates. For microfluidic samples (*top*), prediction error minimizes at three components (RMSEP = 0.29), beyond which overfitting occurs. Dished samples (*bottom*) achieve minimal error at two components (RMSEP = 0.28), reflecting reduced model complexity needed for accurate classification in dished conditions. Right: the PR curve evaluates the trade-off between classification precision and recall at varying decision thresholds. Each data point on the PR curve is a unique threshold between 0 and 1 that was evaluated on validation data.

variability (median RMS = 8.57e−14 N) compared with unsynchronized cells in microfluidic chambers (median RMS = 1.90e−13 N; $p = 0.0001$). Full raw data analysis is provided in Fig. S2. Scores plots, VIP plots, and model tuning plots of RMSEP and PR can be found in the Supporting Material (Figs. S4–S6).

TABLE 1 Confusion matrix for microfluidics-based A549 cells versus U251 samples

Prediction	Reference	
–	microfluidic A549 cells	U251 cells
microfluidic A549 cells	40	9
U251 cells	12	111

This matrix quantifies model performance by comparing predicted classifications (rows) against true biological labels (columns) for all samples in the test set. A total of 172 (120 U251, 52 Microfluidic A549) samples within the test set were run on the PLS-DA model with three components and a threshold of 0.477. Diagonal entries represent correct predictions by the model: 111 U251 cells were accurately identified (bottom right), and 40 A549 microfluidic cells were correctly classified (top left). Off-diagonal entries indicated misclassifications: nine U251 samples erroneously labeled as A549 microfluidic cells (false positives) and 12 A549 recordings incorrectly assigned to U251 by the model (false negatives).

PLS-DA modeling using 202 detected frequency peaks with a two-component model (threshold = 0.463) was applied to the test set containing 151 samples (120 U251, 31 synchronized A549). The confusion matrix and performance metrics are presented below (Tables 5 and 6).

Performance metric calculations obtained an F1 score of 0.83 (Table 6). This F1 score indicated the model performed well at both correctly identifying positive instances and ensuring positive predictions were reliable in determining synchronized A549 cells from unsynchronized U251. Interestingly, the synchronization of the cell cycle does cause a slight improvement in F1 score, being 0.83, when compared with the F1 score of 0.79 in unsynchronized microfluidic chambers (Tables 2 and 6). This supports cell-cycle synchronization in improving the ability to differentiate cell types using CVP.

Viscosity treatment

A549 cells were examined in DMEM with incrementally increased viscosities using agarose: 0.1 (n = 29), 0.2 (n = 30), and 0.3 wt % (n = 27); these samples were modeled against U251 control cells (n = 403).

TABLE 2 Performance metrics for microfluidics A549 cells versus U251 cells

Metric	F1	Accuracy	Sensitivity	Specificity	Recall	Precision
Value	**0.79**	0.88	0.77	0.93	0.77	0.82

The model had a decision threshold of 0.477 with positive values being treated as the microfluidics A549 samples and zero or negative values being treated as U251 cells. The model performed generally good with a precision of 0.82 and recall of 0.77. Additionally, a high specificity of 0.93 indicates the model did well on avoiding false-positive identifications of microfluidic samples. Bold values indicate the key performance metrics emphasized in this study (F1 score, and recall/sensitivity for the positive class), which summarize the model's ability to correctly identify the positive cell population while balancing precision and recall.

Viscosity-treated samples showed statistically significant differences in RMS values compared with A549 cells in untreated DMEM ($p < 0.05$ for all comparisons), with reduced vibrational intensity and decreased data spread. Full raw data analysis, power spectra comparisons, and statistical testing are provided in Fig. S3. Scores plots, VIP plots, and model tuning plots of RMSEP and PR can be found in the Supporting Material (Figs. S7–S9).

For classification analysis, all viscosity-treated samples (total $n = 86$) were combined as a single class and compared against U251 cells. PLS-DA modeling using 180 detected frequency peaks with a two-component model (threshold = 0.414) was applied to the test set containing 145 samples (120 U251, 25 viscosity-treated A549). The confusion matrix and performance metrics are presented below (Tables 7 and 8).

The test set of this viscosity model consisted of a total of 145 samples, where 120 were U251 GBM cells as our control to measure differentiation, and 25 were viscosity-treated A549 cells in microfluidic chambers. Binary classification was performed to distinguish U251 and A549 cells, with A549 cells treated as the positive class and U251 cells as the negative class (Tables 7 and 8). A confusion matrix was generated to visualize the model's ability to differentiate samples within the test set using a previously obtained threshold (Tables 7 and 8).

TABLE 3 Confusion matrix for dished A549 versus U251 samples

Prediction	Reference	
–	dished A549 cells	U251 cells
dished A549 cells	34	5
U251 cells	3	115

This matrix quantified model performance by comparing predicted classifications (rows) against true biological labels (columns) for all samples in the test set. A total of 157 samples (120 U251, 37 dished A549) within the test set were run on the PLS-DA model with two components and a threshold of 0.449. Diagonal entries represent correct predictions by the model: 115 U251 cells were accurately identified (bottom right), and 34 A549 dished cells were correctly classified (top left). Off-diagonal entries indicate misclassifications: five U251 samples erroneously labeled as A549 dished cells (false positives) and three A549 recordings incorrectly assigned to U251 by the model (false negatives).

Performance metric calculations obtained an F1 score of 0.81 (Table 8), suggesting good performance at both correctly identifying positive instances and ensuring positive predictions were reliable in determining viscosity-treated A549 cells from untreated U251. Interestingly, the synchronization of the cell cycle resulted in F1 score improvement, being 0.81, when compared with an F1 score of 0.79 in A549 cells measured in microfluidic channels without synchronization (Tables 2 and 8). This supports the claim that viscosity treatment of cells causes slight improvements in the ability to differentiate cell types using vibrations; this small amount requires further study and may be negligible.

Overall, examining the roles of the sample chamber, cell-cycle synchronization, and viscosity treatment of samples, we determined the largest, most well-defined improvements of discriminatory ability in F1 score arose from the choice of sample chamber (10%). This is then followed by slight improvements in differentiation observed from cell-cycle synchronization (4%) and minor improvements arising from increasing viscosity in cellular medium (2%). These findings support the hypothesis that all experimental considerations should be carefully controlled, as inconsistency can be a source of variability when comparing data recordings. These findings in CVP experiments help pave the way for optimized cellular characterization platforms by presenting a quantitative framework to measure the impact of experimental conditions on CPV-based classification performance.

DISCUSSION

The development of rapid, label-free diagnostic tools represents one of the most pressing challenges in modern precision medicine, particularly for early cancer detection and real-time therapeutic monitoring. Traditional diagnostic approaches rely heavily on biochemical markers, imaging, or invasive tissue sampling, each presenting limitations in terms of cost, time requirements, accessibility, or patient comfort. CVP emerges as a developing approach that harnesses the inherent mechanical vibrations of living

TABLE 4 Performance metrics for dished A549 cells versus U251 cells

Metric	F1	Accuracy	Sensitivity	Specificity	Recall	Precision
Value	**0.89**	0.95	0.92	0.96	0.92	0.87

The model had a decision threshold of 0.449 with positive values being treated as the dished A549 samples, and zero or negative values being treated as U251 cells. The model was very robust overall, producing a high precision and recall of 0.87 and 0.92, indicating it is competent at capturing all instances of dished A549 cells, and keeping the false positive rate low. Bold values indicate the key performance metrics emphasized in this study (F1 score, and recall/sensitivity for the positive class), which summarize the model's ability to correctly identify the positive cell population while balancing precision and recall.

cells, arising from metabolic processes, cytoskeletal dynamics, and membrane fluctuations to extract diagnostic information without the need for external labels or invasive procedures. The fundamental premise underlying CVP encapsulates the ideology of cellular vibrations reflecting the underlying biophysical and biochemical state of cells, with malignant cells exhibiting distinct vibrational signatures due to their altered metabolism, mechanical properties, and intracellular dynamics compared with their healthy counterparts. Our systematic evaluation of experimental parameters provides a methodological foundation necessary for standardizing CVP protocols, thereby facilitating the transition from proof-of-concept studies to pragmatic clinical implementation.

The choice of metrics

The choice to use F1 score and PR plots to determine boundaries places an emphasis on the positive classification of data, as true negative samples are not put into consideration (45,46). F1 scores perform well against imbalanced data sets, typical when dealing with biological samples (45). One of the primary intended applications of CVP is cancer identification, whereby the correct identification of a cellular phenotype is essential (9). It is imperative to have both high recall for capturing all cases where cells are cancerous and high precision in ensuring that all positive cases are correctly identified as cancer without false positives, whereby a positive case has high value. In the decision of model tuning metrics, we selected threshold values with a preference for slightly higher recall values than precision. Practically, when CVP is applied, the method must capture all positive cases of cancer when they do occur and leave some margin for error in the cases of false positives demonstrated by the model. We emphasize the use of F1 scores and PR plots with a bias toward recall values is essential for future studies in CVP. As this is a novel technique in cell vibrations, there are no established F1 metrics for comparison. This manuscript therefore sets a benchmark for future research, providing an initial metric for evaluating subsequent findings.

TABLE 5 Confusion matrix for synchronized A549 versus U251 cells

Prediction	–	Reference synchronized A549 cells	U251 cells
	synchronized A549 cells	26	6
	U251 cells	5	114

This matrix quantifies model performance by comparing predicted classifications (rows) against true biological labels (columns) for all samples in the test set. A total of 151 (120 U251, 31 synchronized A549) samples within the test set were run on the PLS-DA model with two components and a threshold of 0.463. Diagonal entries represented correct predictions by the model: 114 U251 cells were accurately identified (bottom right), and 26 A549 cell-cycle synchronized cells were correctly classified (top left). Off-diagonal entries indicate misclassifications: six U251 samples erroneously labeled as A549 synchronized cells (false positives) and five A549 recordings incorrectly assigned to U251 by the model (false negatives).

Dished versus microfluidics in A549 human alveolar epithelial cells and U251 glioblastoma cells

Containing materials exhibit resonant vibrations. Resonant vibrations can often be characterized by the frequencies they emit. We previously proposed a technique using a polystyrene bead as a detector for vibrational frequencies in the experimental cavity (9). A stiff, rigid material such as a polystyrene bead is less likely to dissipate vibrations due to Young's modulus and viscoelastic properties and is therefore a good choice for a detector. In the present study, we further examined the impacts of the choice of experimental chamber on the VFPs emitted by A549 HAE cells.

When comparing raw data, 173 A549 cells cultured in microfluidic chambers and 129 A549 cells in open-cavity chambers, dished samples demonstrated an overall decreased value of vibrational intensity as indicated by their RMS value (Fig. 1.1, 1.2). This decrease may be associated with the dished samples being an open cavity, thereby dissipating cell vibrations more readily than a closed (microfluidics) cavity where vibrations may reverberate back into the medium. In line with this, dished cells demonstrated a more uniform and overall decreased intensity across their averaged power spectrum, particularly above

TABLE 6 Performance metrics for synchronized A549 cells versus U251 cells

Metric	F1	Accuracy	Sensitivity	Specificity	Recall	Precision
Value	**0.83**	0.93	0.84	0.95	0.84	0.81

The model had a decision threshold of 0.463 with positive values being treated as the synchronized A549 samples and zero or negative values being treated as U251 cells. The model performed generally well with a precision of 0.81 and recall of 0.84, with a slightly higher recall indicating the model did a good job of identifying all instances of synchronized A549 cells. A high specificity of 0.95 indicated the model avoided false-positive identifications of synchronized A549 cells. Bold values indicate the key performance metrics emphasized in this study (F1 score, and recall/sensitivity for the positive class), which summarize the model's ability to correctly identify the positive cell population while balancing precision and recall.

3000 Hz, with a substantially decreased peak at 11,111 Hz (Fig. 1.3).

Two models were developed using different cell types and chamber configurations. For the first model, data were collected from 173 A549 cells cultured in microfluidic chambers and compared against 403 U251 control cell recordings. The second model utilized recordings from 129 A549 cells in dished open cavity chambers, together with the same 403 U251 cell control recordings. From PLS-DA modeling, we sought to identify which of the two models demonstrated a greater separability between the two cell types and thereby would allow identification of which condition best differentiates the cell types. PLS-DA scores demonstrated clear differences in clustering: microfluidic samples spread more widely across the components, and dished samples clustered tightly across the first, second, and third components (Fig. 4). Furthermore, it was observed from VIP plots that the frequencies of 338, 1480, and 1540 Hz provided a significant proportion of the variance found in the first principal component for microfluidic samples, whereas 40,035, 49,539, and 48,805 Hz played a substantial role in dished samples (Fig. S2). This interesting finding indicates that the vibrations detected by OT are substantially different between microfluidic and dished samples, which may be attributed to chamber geometry or thickness of material rather than a product of the cells themselves. This shows the importance of geometry, not just the susceptibility to environmental noise, as different sampling chamber geometries likely amplify or dampen a unique set of frequencies.

After model tuning and threshold selection, PLS-DA values were predicted on the test set, demonstrating an F1 score of 0.79 for the microfluidic-based model and F1 score of 0.89 for the dished sample (Table 1, 2, 3, and 4). This suggests that A549 cells in dished chambers were more effectively differentiated from U251 cells than their microfluidic counterparts. An F1 score of 0.89 reflects a strong balance between precision and recall, indicating that the model not only correctly identifies most true cell-type distinctions but also minimizes false classifications. In practical terms, this performance underscores the robustness and discriminative reliability of the CVP-derived features, supporting the potential of vibrational data to serve as a reproducible, label-free basis for distinguishing between cell phenotypes. Using single-cell vibrational data, our model demonstrates CVP data can be used alongside PLS-DA to generate models with a high level of discriminative reliability to distinguish between distinct cell types.

TABLE 7 Confusion matrix for viscosity-treated A549 versus U251 cells

Prediction	Reference	
–	viscosity-treated A549	U251 cells
viscosity-treated A549	21	6
U251 cells	4	114

A total of 145 (120 U251, 25 viscosity-treated A549) samples within the test set were run on the PLS-DA model with two components and a threshold of 0.414. Diagonal entries represented correct predictions by the model: 114 U251 cells were accurately identified (bottom right), and 21 A549 viscosity-treated cells were correctly classified (top left). Off-diagonal entries indicate misclassifications: six U251 samples erroneously labeled as A549 viscosity-treated cells (false positives) and four A549 recordings incorrectly assigned to U251 by the model (false negatives).

Synchronization of the cell cycle

Different stages of the cell cycle are characterized by dynamic activity patterns and changes to cellular characteristics (26). Oscillatory patterns change with metabolic states in *Saccharomyces cerevisiae* and have been linked to mitotic exit and budding (21). These oscillations are not just a consequence of cell-cycle progression but likely also play a coordinating role in cell division (26). We examined the role of the cell cycle on CVP experiments. A PLS-DA model was developed consisting of 105 synchronized A549 cells and 403 U251 GBM cells as control.

To study the role of the cell cycle and its impact on single-cell VFPs, serum was gradually deprived from cell medium. Theoretically, serum deprivation arrests cells in the G_0/G_1 phase of the cell cycle resultant from lack of growth factor. Consistent with this ideology, A549 cells synchronized in the G_0/G_1 phase were found to have statistically significant differences in

TABLE 8 Performance metrics for viscosity-treated A549 cells versus U251 cells

Metric	F1	Accuracy	Sensitivity	Specificity	Recall	Precision
Value	**0.81**	0.93	0.84	0.95	0.84	0.78

The model had a decision threshold of 0.414 with positive values being treated as viscosity-treated A549 samples and 0 or negative values being treated as U251 cells. The model performed generally good with a precision of 0.78 and recall of 0.84, with a higher recall indicating the model performed well at identifying all instances of viscosity-treated A549 cells. Additionally, a high specificity of 0.95 indicated the model avoided false-positive identifications of viscosity-treated A549 cells. Bold values indicate the key performance metrics emphasized in this study (F1 score, and recall/sensitivity for the positive class), which summarize the model's ability to correctly identify the positive cell population while balancing precision and recall.

their VFPs from A549 cells that did not undergo serum deprivation ($p < 0.0001$) (Fig. S2.1). Although differing metabolic activities throughout the cell cycle have been previously described in the literature, oscillatory spectra corresponding with these changes are a novel discovery. This may prove foundational for future studies exploring cell vibrations to create more consistent samples and eliminate inaccurate VFPs owing to different stages of the cell cycle.

From PLS-DA modeling, score plots demonstrated synchronized and unsynchronized samples tended to cluster to opposite ends of the first and third components (Fig. S4). VIP plots that demonstrated frequencies of 40,033 Hz, 11,111 Hz, 1498 Hz, and 320 Hz provided the greatest proportion of the variance found in the first principal component (Fig. S5). After model tuning and threshold selection, a PLS-DA model predicted on the test set demonstrated an F1 score of 0.83 (Table 6). This model demonstrated improvement in F1 score of 0.79 from A549 cells in unsynchronized microfluidics chambers (Table 2). This indicated an improved ability to correctly identify A549 cell samples from a test set containing both A549 and U251 cells as proven by the F1 score (Tables 2 and 6). The comparison was performed against cells in microfluidics samples as unsynchronized cells were recorded in microfluidic chambers. Interpretations from the model discovered measurable improvements in PLS-DA predictability in CVP experiments when synchronizing cells in the G_0/G_1 phase of the cell cycle. In the clinical setting, unsynchronized cells are commonly extracted from biopsy. Without synchronization, a distinction between cell types can be obtained; however, our findings demonstrate this approach would result in less confidence in oscillatory differentiability.

Viscosity

Cells suspended in medium are subject to Brownian motion (23). This may negatively impact cell vibrational recordings through environmental "noise" but can also add value to oscillatory spectra as cells utilize Brownian motion through Brownian motors (22). We previously established that Brownian motion is influenced by medium viscosity, and its ability to impact resultant cell vibrational recordings is intriguing.

To study the role of medium viscosity and its impact on VFPs in A549 cells, differing concentrations of agarose were added to DMEM. RMS values were collected for each spectral sample and compared across groups. When comparing untreated A549 cell samples to viscosity-treated A549 cells, statistically significant differences were observed for each group (Fig. S3.2). The differences observed from a Welch's *t*-test between untreated and treated with 0.1 wt % were $p = 0.0004$, between untreated and 0.2 wt % was $p < 0.0001$, and for 0.3 wt %, $p = 0.0326$ (Fig. S3.2). Additionally, when comparing between treated conditions, no statistically significant differences were observed under any condition (Fig. S3.2). Clearly, differences exist in the vibrations collected within differing cell media viscosities. Furthermore, these differences appear binary, indicating that the observed vibrational differences are driven by the presence of viscosity alteration itself, rather than the degree of viscosity change, as significance was only observed between untreated and treated samples but not among the treatment levels. This may be tied to cellular interaction with the agarose that was added resulting in a different set of vibrations or the agarose itself dampening the vibrations that we observe on the OT.

From PLS-DA modeling comparing viscosity-treated A549 cells and non-viscosity-treated U251 cells, score plots demonstrated the projection of data samples onto model components (Fig. S7). From the first and second components, untreated microfluidics samples demonstrated substantially greater values and therefore contributed more overall variance to the components, whereas no significant trend was observed in the third component (Fig. S7). We examined the individual frequencies of the model regarding variance in each of the frequencies represented in a respective component (Fig. S8). From VIP plots, 11,111Hz, 1340Hz, and 1464 Hz significantly developed the PLS-DA model (Fig. S8). These frequencies require further study and may be of value for the differentiation of different cell types or may

have ties to cell micromechanics. After model tuning and threshold selection, a PLS-DA model was predicted on the test set and demonstrated an F1 score of 0.81 (Table 8). This F1 score is a marginal improvement from the F1 score of A549 cells in microfluidic chambers that were not viscosity treated, being 0.79 (Table 2). This suggested slight improved ability to correctly differentiate between A549 and U251 cells in a test set containing both U251 and A549 cells, as proven by the F1 score when compared with previous models (Tables 2 and 8). We determined slight improvements in PLS-DA model predictability in CVP experiments when increasing cellular medium viscosity using agarose.

Calibration

The Nanotracker 2 system utilizes a QPD photodetector system to measure signals (47). OT typically use photodetectors to measure the position of a trapped particle, producing raw voltage signals (31). However, for these measurements to be meaningful and provide relevant information for cellular properties and mechanisms with relation to force, two key conversions are necessary (31). These conversions are based on the understanding that a harmonic trap acts as a Hookean Spring, whereby $F = -kx$ (31).

1. The voltage signals must be translated into actual physical displacements, usually measured in nanometers and referred to as trap sensitivity. This serves as the displacement to be used in Hooke's law.
2. To calculate the force acting on the particle, the trap stiffness (expressed in piconewtons per nanometer) needs to be determined.

Most OT setups require specific calibration procedures to accurately determine these parameters. These calibrations are crucial for converting raw voltage data into physically meaningful measurements of position and force (31). The method used on the Nanotracker 2 involves the fitting of a Lorentzian function to the power spectrum of Brownian motion of the cell, which is a commonly used approach to calibration of optical traps (48,49). The Lorentzian function of the power spectra is described as follows (48,49):

$$S_{xx}(f) = \frac{k_B T}{\pi^2 \gamma \left(f^2 + f_c^{\,2}\right)}$$

Here, k_B is boltzmann's constant, T is temperature, and γ is the coefficient of hydrodynamic drag (48,49). γ can be determined for a spherical particle with the stokes relation $\gamma = 3\pi\eta d$, whereby η is viscosity of medium, and d is particle diameter (50). Next, f_c is the cornering frequency, which is largely determinant of the shape of the Lorentzian function (31,48,49). f_c represents the frequency at which power drops to half of its maximum value. f_c can be determined using the following formula (48,49):

$$f_c = \frac{k}{2\pi\gamma}$$

From this formula, we can extract the trap stiffness, k, which can then be directly used in the calculation of force. Typically, this calibration would be performed by collecting the power spectra of the Brownian motion of your sample and then fitting the above Lorentzian function on the power spectrum with different values for cornering frequency and selecting the value of best fit (49). The fitting process attempts to minimize the difference between experimental data and theoretical Lorentzian values (49). This calibration would need to be performed in each dimension to be analyzed. For the sake of simplicity, we have only examined the X dimension. Next, the technique behind calculating sensitivity for converting from distance to force is highly dependent upon the OT system and the detector used, whether it is a CCD camera measuring distance or a position sensitive detector, such as a QPD (51). Further information is available in the literature (48,49,51). Considering hydrodynamic drag is dependent upon medium viscosity, the importance of measurements examining the role of viscosity in calculated values for CVP studies is evident. Furthermore, the role of cell diameter is also evident from the equation and can provide a compounding factor whereby diameter must be measured for each experiment, and cell shape is often not perfectly spherical.

Limitations of this study

This study examined only two immortalized cancer cell lines (A549 and U251). Although these provide well-characterized models for method development, their behavior may not represent that of primary or nonmalignant cells, or of many other cell lines. Future work should extend CVP analyses to additional cancer types, normal epithelial controls, and primary patient-derived cells to validate generalizability and clinical relevance.

Secondly, although increased agarose concentrations were associated with reduced data spread and distinct spectral features, we did not assess the long-term viability of cells in these media. Although agarose is widely used, it may impose mechanical or metabolic

stress on cells when used at an elevated concentration. The reduced vibrational variability observed in viscosity-treated conditions could therefore result from either improved signal isolation or early stages of cell death. Future studies are needed to directly assess cell survivability under increased medium viscosity to clarify whether the spectral changes reflect altered mechanics or compromised viability.

Additionally, a challenge in our current analysis was the presence of 1/f noise within our OT setup, which limited our analysis of biological signals in the low-frequency domain. We attribute this background interference to the inherent complexity of our Nanotracker 2 system, where multicomponent architecture may increase susceptibility to environmental coupling. Future investigations utilizing more rigid, simplified experimental configurations could effectively mitigate these noise artifacts, thereby unlocking the potential for detailed analysis within these lower frequency bands.

CONCLUSIONS

Experimental chamber impact

The choice between dished and microfluidic chambers substantially affects the VFPs of A549 cells. Cells placed within Petri-dishes exhibited a statistically significant decrease in overall vibrational intensity compared with microfluidic chambers, likely due to the open nature of the dished cavity allowing for greater dissipation of vibrations. This was evidenced by a p-value <0.0001 and a PLS-DA model with an F1 score of 0.89 when compared with the VFP of microfluidics chambers at 0.79, indicating an increased ability to differentiate between the two conditions based on vibrational data. From these robust statistical findings, we infer cell vibrational recordings are best obtained in open-cavity Petri dish chambers to enable accurate and reproducible cell spectra identification for the purposes of cell phenotyping.

Cell-cycle synchronization

Synchronizing cells in the G_0/G_1 phase through serum deprivation resulted in a significant difference in VFPs when compared with unsynchronized conditions. Synchronized cells demonstrated less spread in vibrational data, suggesting more uniform metabolic activity tied to the cell-cycle stage. The PLS-DA model for this comparison also increased from baseline, having an F1 score of 0.83 when compared with the baseline of 0.79, indicating an improved ability to categorize cells based on their synchronization status. Our findings demonstrate evidence to suggest that accuracy of cell VFPs is enhanced under cell-cycle-synchronized conditions, standardizing metabolic activity, and this may permit clear identification between and within cell types.

Medium viscosity

Increasing the viscosity of the cell medium with agarose had a slight impact on VFPs. Higher viscosity medium resulted in less spread in RMS values, potentially due to the medium's ability to dampen large oscillations. The frequency domain analysis eliminated certain vibrational peaks from viscosity samples when compared with untreated counterparts. Additionally, PLS-DA modeling demonstrated viscosity-treated samples could be differentiated from untreated ones with an improved F1 score of 0.81 when compared with baseline of 0.79. This indicates models can be developed with an improved ability to differentiate between the viscosity-treated and nontreated samples based on vibrational data.

In summary, the study demonstrates that the experimental setup, including the choice of chamber, cell-cycle synchronization, and medium viscosity, all influence the vibrational profiles of A549 cells and should be accounted for at differing levels of importance. Among these, chamber geometry exerted the strongest influence on VFP variability, followed by cell-cycle synchronization, whereas medium viscosity had a comparatively modest but measurable effect. The PLS-DA models developed from these experiments show varying degrees of success in identifying these conditions, where the highest performance observed was in dished chambers with F1 score of 0.89. Future studies should combine all three findings from this work and examine whether the combined impact of dish chambers, cell-cycle synchronization, and increasing medium viscosity can synergistically work together to improve differentiation, or if they act on mechanisms that are not mutually exclusive. This study underscores the importance of controlling experimental variables in CVP studies and the potential of CVP as a tool for identifying cellular states and differentiation while providing a technique to measure the impact of experimental variables. Collectively, this work establishes a framework for how experimental parameters shape cell vibrational behavior, positioning CVP as a powerful quantitative tool for probing cellular states, enhancing diagnostic discrimination, and advancing the translation of vibration-based phenotyping toward the ultimate goal of clinical applications such as cancer screening, drug response monitoring, metabolic profiling, antimicrobial resistance detection, and real-time assessment of cellular health in diverse research and clinical settings.

DATA AND CODE AVAILABILITY

All force spectroscopy data used in this article have been deposited at the Harvard Dataverse under the accession identifier https://doi.org/10.7910/DVN/G7ZSG7 and are publicly available as of the article publication date.

ACKNOWLEDGMENTS

We acknowledge Nasir Osman for his support in developing the statistical processing software in its early stages. We acknowledge Dr. Brandy Pilapil for devoting her expertise with optical tweezers to this study. This study was funded by an NSERC discovery grant to M.A.

AUTHOR CONTRIBUTIONS

Experimental approach was performed by J.J.T and A.A-K'A. Writing was performed by A.A-K'A. and T.P. Development of the software and statistical processing used in the project was by A.A-K'A. and F.F. Supervision of the project was performed by M.A. and F.F.

DECLARATION OF INTERESTS

The authors declare no competing interests.

SUPPORTING MATERIAL

Supporting Material can be found online at https://doi.org/10.1016/j.bpr.2026.100252.

REFERENCES

1. Peng, Y., J. Zhang, …, Q. Zhang. 2023. Nanomechanical vibration profiling of oocytes. *Nano Res.* 16:2672–2681. https://doi.org/10.1007/s12274-022-4439-7.
2. Nelson, S. L., D. T. Proctor, …, G. R. Sutherland. 2017. Vibrational Profiling of Brain Tumors and Cells. *Theranostics.* 7:2417–2430. https://doi.org/10.7150/thno.19172.
3. Kasas, S., F. S. Ruggeri, …, G. Longo. 2015. Detecting nanoscale vibrations as signature of life. *Proc. Natl. Acad. Sci. USA.* 112:378–381. https://doi.org/10.1073/pnas.1415348112.
4. Zhou, J., J. Huang, …, Y. Wang. 2023. Fiber-integrated cantilever-based nanomechanical biosensors as a tool for rapid antibiotic susceptibility testing. *Biomed. Opt. Express.* 14:1862–1873. https://doi.org/10.1364/BOE.484015.
5. Pelling, A. E., S. Sehati, …, J. K. Gimzewski. 2005. Time dependence of the frequency and amplitude of the local nanomechanical motion of yeast. *Nanomedicine.* 1:178–183. https://doi.org/10.1016/j.nano.2005.04.002.
6. Wu, S., X. Liu, …, X. Wu. 2016. Quantification of cell viability and rapid screening anti-cancer drug utilizing nanomechanical fluctuation. *Biosens. Bioelectron.* 77:164–173. https://doi.org/10.1016/j.bios.2015.09.024.
7. Stupar, P., W. Chomicki, …, S. Kasas. 2017. Mitochondrial activity detected by cantilever based sensor. *Mech. Sci.* 8:23–28. https://doi.org/10.5194/ms-8-23-2017.
8. Longo, G., L. Alonso-Sarduy, …, S. Kasas. 2013. Rapid detection of bacterial resistance to antibiotics using AFM cantilevers as nanomechanical sensors. *Nat. Nanotechnol.* 8:522–526. https://doi.org/10.1038/nnano.2013.120.
9. Al-Khaz'Aly, A., S. Ghandorah, …, M. Amrein. 2025. A Comprehensive Method to Analyze Single Cell Vibrations. *Biophys. J.* 124:77–92. https://doi.org/10.1016/j.bpj.2024.11.003.
10. Willaert, R. G., P. Vanden Boer, …, S. Kasas. 2020. Single yeast cell nanomotions correlate with cellular activity. *Sci. Adv.* 6:eaba3139. https://doi.org/10.1126/sciadv.aba3139.
11. Rosłoń, I. E., A. Japaridze, …, F. Alijani. 2022. Probing nanomotion of single bacteria with graphene drums. *Nat. Nanotechnol.* 17:637–642. https://doi.org/10.1038/s41565-022-01111-6.
12. Pesce, G., P. H. Jones, …, G. Volpe. 2020. Optical tweezers: theory and practice. *Eur. Phys. J. Plus.* 135:949. https://doi.org/10.1140/epjp/s13360-020-00843-5.
13. Zhang, H., and K.-K. Liu. 2008. Optical tweezers for single cells. *J. R. Soc. Interface.* 5:671–690. https://doi.org/10.1098/rsif.2008.0052.
14. Neuman, K. C., and A. Nagy. 2008. Single-molecule force spectroscopy: optical tweezers, magnetic tweezers and atomic force microscopy. *Nat. Methods.* 5:491–505. https://doi.org/10.1038/nmeth.1218.
15. Sarshar, M., W. T. Wong, and B. Anvari. 2014. Comparative study of methods to calibrate the stiffness of a single-beam gradient-force optical tweezers over various laser trapping powers. *J. Biomed. Opt.* 19:115001. https://doi.org/10.1117/1.JBO.19.11.115001.
16. Puerto-Belda, V., J. J. Ruz, …, J. Tamayo. 2024. Measuring Vibrational Modes in Living Human Cells. *PRX Life.* 2:013003. https://doi.org/10.1103/PRXLife.2.013003.
17. Czerwinski, F., A. C. Richardson, and L. B. Oddershede. 2009. Quantifying Noise in Optical Tweezers by Allan Variance. *Opt. Express.* 17:13255–13269. https://doi.org/10.1364/OE.17.013255.
18. Jia, D., J. Hamilton, …, A. Goonewardene. 2007. The time, size, viscosity, and temperature dependence of the Brownian motion of polystyrene microspheres. *Am. J. Phys.* 75:111–115. https://doi.org/10.1119/1.2386163.
19. Topham, J. J. 2021. Cell Vibrational Profiling (CVP) Using Optical Tweezers to Improve Tumour Diagnosis: A Novel Methodological Approach. Masters Thesis. University Of Calgary.
20. Ma, H., J. Jimenez, and R. Rajagopalan. 2000. Brownian Fluctuation Spectroscopy Using Atomic Force Microscopes. *Langmuir.* 16:2254–2261. https://doi.org/10.1021/la991059q.
21. Al-Khaz'Aly, A. 2025. A Novel Statistical and Experimental Framework for Real-Time Single Cell Classification using Cell Vibrations. Doctoral Thesis. University of Calgary.
22. Astumian, R. D., and P. Hänggi. 2002. Brownian Motors. *Phys. Today.* 55:33–39. https://doi.org/10.1063/1.1535005.
23. Tsekov, R., and M. C. Lensen. 2013. Brownian Motion and the Temperament of Living Cells. *Chin. Phys. Lett.* 30:070501. https://doi.org/10.1088/0256-307X/30/7/070501.
24. Codling, E. A., M. J. Plank, and S. Benhamou. 2008. Random walk models in biology. *J. R. Soc. Interface.* 5:813–834. https://doi.org/10.1098/rsif.2008.0014.
25. Frey, E., and K. Kroy. 2005. Brownian motion: a paradigm of soft matter and biological physics. *Ann. Phys.* 517:20–50. https://doi.org/10.1002/andp.200551701-303.
26. Zylstra, A., and M. Heinemann. 2022. Metabolic dynamics during the cell cycle. *Curr. Opin. Syst. Biol.* 30:100415. https://doi.org/10.1016/j.coisb.2022.100415.
27. Ahn, E., P. Kumar, …, T. Shlomi. 2017. Temporal fluxomics reveals oscillations in TCA cycle flux throughout the mammalian cell cycle. *Mol. Syst. Biol.* 13:953. https://doi.org/10.15252/msb.20177763.
28. Foster, K. A., C. G. Oster, …, K. L. Audus. 1998. Characterization of the A549 Cell Line as a Type II Pulmonary Epithelial Cell Model for Drug Metabolism. *Exp. Cell Res.* 243:359–366. https://doi.org/10.1006/excr.1998.4172.

29. Lauand, C., E. L. Niero, …, G. M. Machado-Santelli. 2015. Cell cycle synchronization and BrdU incorporation as a tool to study the possible selective elimination of ErbB1 gene in the micronuclei in A549 cells. *Braz. J. Med. Biol. Res.* 48:382–391. https://doi.org/10.1590/1414-431x20144262.

30. Carlsson, J. 1978. Physical and nutritional factors in gel culture of mammalian cells. *In Vitro.* 14:860–867. https://doi.org/10.1007/BF02616156.

31. Bustamante, C. J., Y. R. Chemla, …, M. D. Wang. 2021. Optical tweezers in single-molecule biophysics. *Nat. Rev. Methods Primers.* 1:25. https://doi.org/10.1038/s43586-021-00021-6.

32. Ramakrishnan, K., B. Ajitha, and Y. Ashok Kumar Reddy. 2023. Review on metal sulfide-based nanostructures for photodetectors: From ultraviolet to infrared regions. *Sens Actuators A Phys.* 349:114051. https://doi.org/10.1016/j.sna.2022.114051.

33. Crecraft, D. I., and S. Gergely. 2002. Signals and signal processing. *In* Analog Electronics Elsevier, pp. 13–71.

34. Varmuza, K., and P. Filzmoser. 2016. Introduction to Multivariate Statistical Analysis in Chemometrics. CRC Press.

35. van Brakel, J. P. G. 2014. Robust peak detection algorithm using z-scores. https://stackoverflow.com/questions/22583391/peak-signal-detection-in-realtime-timeseries-data.

36. Shannon, C. E. 1949. Communication in the Presence of Noise. *Proc. IRE.* 37:10–21. https://doi.org/10.1109/JRPROC.1949.232969.

37. Craig, A., O. Cloarec, …, J. C. Lindon. 2006. Scaling and Normalization Effects in NMR Spectroscopic Metabonomic Data Sets. *Anal. Chem.* 78:2262–2267. https://doi.org/10.1021/ac0519312.

38. Worley, B., and R. Powers. 2013. Multivariate Analysis in Metabolomics. *Curr. Metabolomics.* 1:92–107. https://doi.org/10.2174/2213235X11301010092.

39. Gazi, O. 2018. Understanding Digital Signal Processing. Springer Singapore: Singapore.

40. Ruiz-Perez, D., H. Guan, …, G. Narasimhan. 2020. So you think you can PLS-DA? *BMC Bioinf.* 21:2. https://doi.org/10.1186/s12859-019-3310-7.

41. Mevik, B.-H., and R. Wehrens. 2007. The pls package: principal component and partial least squares regression in R. *J. Stat. Softw.* 18:1–24. https://doi.org/10.18637/jss.v018.i02.

42. Bi, K., D. Zhang, …, Y. Huang. 2019. A PLSR Model for Consumer Preference Prediction of Yoghurt from Sensory Attributes Profiles. *Comput. Chem. Eng.* 46:1477–1482.

43. Mevik, B., and H. R. Cederkvist. 2004. Mean squared error of prediction (MSEP) estimates for principal component regression (PCR) and partial least squares regression (PLSR). *J. Chemom.* 18:422–429. https://doi.org/10.1002/cem.887.

44. Davis, J., and M. Goadrich. 2006. The relationship between Precision-Recall and ROC curves. *In* Proceedings of the 23rd international conference on Machine learning - ICML '06 ACM Press: New York, New York, USA, pp. 233–240.

45. Christen, P., D. J. Hand, and N. Kirielle. 2024. A Review of the F-Measure: Its History, Properties, Criticism, and Alternatives. *ACM Comput. Surv.* 56:1–24. https://doi.org/10.1145/3606367.

46. Jeni, L. A., J. F. Cohn, and F. De La Torre. 2013. Facing Imbalanced Data—Recommendations for the Use of Performance Metrics. *In* 2013 Humaine Association Conference on Affective Computing and Intelligent Interaction IEEE, pp. 245–251.

47. JPK Instruments, A. G. 2016. NanoTrackerTM 2 Force-Sensing Optical Tweezers. JPK Instruments: Berlin, Germany.

48. Neuman, K. C., and S. M. Block. 2004. Optical trapping. *Rev. Sci. Instrum.* 75:2787–2809. https://doi.org/10.1063/1.1785844.

49. Berg-Sørensen, K., and H. Flyvbjerg. 2004. Power spectrum analysis for optical tweezers. *Rev. Sci. Instrum.* 75:594–612. https://doi.org/10.1063/1.1645654.

50. Pesce, G., G. Rusciano, …, E. Ricca. 2014. Surface charge and hydrodynamic coefficient measurements of Bacillus subtilis spore by optical tweezers. *Colloids Surf. B Biointerfaces.* 116:568–575. https://doi.org/10.1016/j.colsurfb.2014.01.039.

51. Gieseler, J., J. R. Gomez-Solano, …, G. Volpe. 2021. Optical tweezers — from calibration to applications: a tutorial. *Adv. Opt. Photonics.* 13:74. https://doi.org/10.1364/AOP.394888.